https://doi.org/10.5194/egusphere-2022-21
Preprint. Discussion started: 28 March 2022

Aerosol Optical Properties of Extreme Global Wildfires and Estimated Radiative Forcing with GCOM-C SGLI

Kazuhisa Tanada[1,*], Hiroshi Murakami[1], Tadahiro Hayasaka[1,2], and Mayumi Yoshida[3]

[1]Earth Observation Research Center (EORC), Japan Aerospace Exploration Agency (JAXA), Tsukuba, Ibaraki 305-8505, Japan
[2]Center for Atmospheric and Oceanic Studies, Tohoku University, Sendai, Miyagi 980-8577, Japan
[3]Remote Sensing Technology Center of Japan (RESTEC), Minato, Tokyo 105-0001, Japan

Correspondence: Kazuhisa Tanada (tanada.kazuhisa@jaxa.jp)

Abstract. Wildfires damage land ecosystems and significantly impact the atmosphere by releasing large amounts of CO_2 and aerosols. Aerosols, in particular, have a radiative forcing potential that perturbs the global radiation balance. Therefore, understanding their optical properties is essential to estimate the radiative forcing for predicting the climatic impact due to burning. The Global Change Observation Mission—Climate, or GCOM-C (SHIKISAI), is a polar-orbit satellite launched by JAXA on 23 December 2017. This study analyzed wildfires in the Amazon, Angola, Australia, California, Siberia, and Southeast Asia that occurred after 2018 using data from the GCOM-C satellite obtained with the Second-generation Global Imager (SGLI), a multi-band optical imaging radiometer. We compared the aerosol optical properties of Ångström Exponent (AE) and Single Scattering Albedo (SSA) and found that their distributions are different for each region. In addition, the negative correlations are found in the Amazon, Angola, Siberia, and Southeast Asia when we locally fitted the AE and SSA relationship for each wildfire by a linear function. This is likely due to the effect of hygroscopic growth (SSA becomes larger with water uptake), considering the difference in relative humidity in the six regions, and the significant behavior of the aerosol aging. We also found that the relationship between SSA and relative humidity varies depending on the type of the burned vegetation. For the needle-forest-dominated group, a higher SSA is observed in the range from 40% to 70% of relative humidity than the broad forest-dominated group. This global investigation of the aerosol optical properties reveals that their characteristics differ due to regional differences such as relative humidity and vegetation type. Thus, the regional characteristics and the aging effect of biomass-burning aerosols must be considered in model predicting. Moreover, we estimated the net incoming radiation at the top of the atmosphere during the intense fire periods to understand the impact of the direct effect of biomass burning aerosols on radiative forcing. The estimates show a significant negative radiative forcing (i.e., a cooling effect) over the ocean (-78 and -96 Wm^{-2} in Australia and California, respectively). In contrast, small values are observed over land (~ -10 Wm^{-2} for all six regions). This suggests that the radiative forcing depends on the region of the wildfire plumes. Therefore, taking the regional characteristics of the optical property and surface reflectance into account is necessary to estimate the effect on radiative forcing and future impacts of a short-lived climate forcer from wildfires.

https://doi.org/10.5194/egusphere-2022-21
Preprint. Discussion started: 28 March 2022

1 Introduction

Wildfires affect Earth's system processes, including weather and climate changes, impacting atmospheric conditions on various spatial and temporal scales through emissions of gases, particles, water, and heat. In recent decades, although CO_2 emissions from savanna and cropland fires have decreased in Africa due to fire suppression and the landscape fragmentation associated with increases in population density (van der Werf et al., 2017; Arora and Melton, 2018), large wildfires have increased globally. This is related to an increase in temperature, sunshine duration, length of episodes without precipitation, and decrease in relative humidity (Gillett et al., 2004; Reinhard et al., 2005; Dennison et al., 2014). These observations suggest that future extreme weather conditions, such as droughts and heat waves, may be brought about by climate change and could increase fire risk.

About 70 % of the emissions from biomass burning are CO_2, which is the most significant contributor to the total radiative forcing and global warming. Incidentally, the net radiation of CO_2 is almost canceled out by plant absorption, accounting for the vegetation regrowing on a decadal time scale except for the peat fires and deforestation (van der Werf et al., 2017). The remaining 30 % are water, CO, and various particles (Council, 2004). Smoke particles from wildfires are composed primarily of organic material (e.g., organic carbon) and black carbon. According to the IPCC 5th Assessment Report (Stocker et al., 2013), the impact of the aerosols emitted from wildfires on the climate is still controversial because they have both positive and negative radiative forcing, depending on the components. Black carbon leads to positive forcing because it absorbs the entire solar spectrum and heats the air. Organic carbon reflects solar radiation and causes a negative forcing. Stocker et al. (2013) reported that radiative forcing of black carbon and organic carbon of biomass burning during the Industrial Era were 0.20 and -0.20 Wm^{-2}, respectively. Generally, aerosols have direct radiative forcing (scattering and absorbing solar and infrared radiation in the atmosphere) and indirect radiative forcing (altering the formation and precipitation efficiency of liquid water, ice, and mixed-phase clouds). Considering the aerosol indirect radiative forcing due to aerosol-cloud interactions, which averaged -0.45 (-1.2 to 0.0) Wm^{-2}, the net radiative forcing of biomass burning aerosols is assumed to be negative. However, there are still significant estimation errors, and it is difficult to conclude the extent of the impact of wildfires on global warming.

To evaluate the impact of aerosol absorption and scattering on climate more precisely, detailed studies of the optical properties related to aerosol particles' size distribution and chemical composition are essential (e.g., Yamamoto and Tanaka, 1972). Generally, the size distribution of the biomass burning aerosol is thought to be dominated by coarse mode (Eck, 1999). In Canada, the median radius of the volume size distribution was reported from 0.20 to 0.25 $\mu\mathrm{m}$ in observations at 440 nm when AOT > 1.0. In Amazon, it was reported to be ~ 0.17 $\mu\mathrm{m}$ by using AErosol RObotic NETwork (AERONET) retrievals (Eck et al., 2009). The Single Scattering Albedo (SSA), which is defined as the ratio of scattering to total extinction, varied from 0.91 to 0.99 at 440 nm in Alaska and Siberia wildfires (Eck et al., 2009; Zhuravleva et al., 2017). These high SSA results (i.e., the small imaginary part of the refractive index) imply a low black carbon fraction probably due to predominantly smoldering combustion. In this boreal forest case, the direct radiative effect efficiency at the top of the atmosphere (TOA) is calculated from -50 to -20 Wm^{-2}. Chang et al. (2021) also reported negative radiative forcing between -14.8 and -17.7 Wm^{-2} in Australia using Moderate Resolution Imaging Spectroradiometer (MODIS) and AERONET data that is the same order of mag-

https://doi.org/10.5194/egusphere-2022-21
Preprint. Discussion started: 28 March 2022

nitude as volcanic eruptions radiative cooling. In addition, the negative shortwave radiative forcing of biomass burning aerosol was enhanced during the aging process by increasing the SSA (Shi et al., 2019).

Previous studies have focused on local fire phenomena, but there have been few systematic analyses of extreme fires based on satellite data. In this study, we investigated the recent extreme wildfires in six regions. We analyzed space-based aerosol optical properties, such as aerosol optical thickness (AOT), SSA, and Ångström exponent (AE), obtained by the Second generation GLobal Imager (SGLI) onboard Global Change Observation Mission – Climate (GCOM-C) satellite. The AOT indicates the amount of aerosols distributed in the air column from Earth's surface to the top of the atmosphere. In general, a large AOT can be observed near cities (urban haze), deserts (dust), and wildfires (smoke particles) and so on. AE describes the wavelength variation in aerosol extinction, including absorption and scattering, which is approximated as the power-law relation $\tau = \tau_1 \lambda^{-\alpha}$, where τ is AOT, τ_1 is AOT at a wavelength of 1 μm, λ is the wavelength, and α is AE (Ångström, 1929). It is also known that the lower the AE, the larger the size of the particles in general (Schuster et al., 2006). Besides, we also evaluate the radiative forcing effect for each extreme wildfire calculated from GCOM-C SGLI's radiance at TOA data. These results might be helpful to understand the impact of wildfires on climate change.

We present the details of the satellite data and analysis data in Section 2. Our analysis results are presented in Section 3. The discussion and conclusions are presented in Section 4. Throughout this paper, the errors correspond to the 1 σ confidence level.

2 Data and Methods

2.1 GCOM-C satellite data

GCOM-C, launched in December 2017 by the Japan Aerospace eXploration Agency (JAXA), is a polar-orbiting satellite carrying a imaging sensor named SGLI. SGLI observes with a multi-wavelength optical radiometer that has 19 observation wavelength bands from near-ultraviolet to thermal infrared and has characteristic functions, such as polarization, multi-directional, and near-ultraviolet observation.

We used the aerosol optical properties product (Ver.2 ARNP) (Yoshida, 2020) retrieved by SGLI non-polarization channels. This aerosol product contains AOT at 500 nm, AE at 380 nm and 500 nm, and SSA at 380 nm, with a spatial resolution of 1 km. In addition, the radiance at TOA product (Ver.2 LTOA) (Takaku, 2020), which has a spatial resolution of 250 m, was used to estimate the net incoming solar radiation to the Earth's surface. The atmospherically corrected surface reflectance product (Ver.2 RSRF) (Murakami, 2020) was also used to compare the difference in the land surface albedos for the wildfire sites. To investigate the hotspot locations of wildfires, we used the SGLI's research product (WFRP: WildFire Radiation Power) that algorithm can detect the hotspots using the thermal infrared channels (10.8, 12.0 μm) with 250 m spatial resolution. This work focused on the global extreme wildfire events from January 2018 to July 2021, as shown in Table 1 and Fig. 1.

https://doi.org/10.5194/egusphere-2022-21
Preprint. Discussion started: 28 March 2022

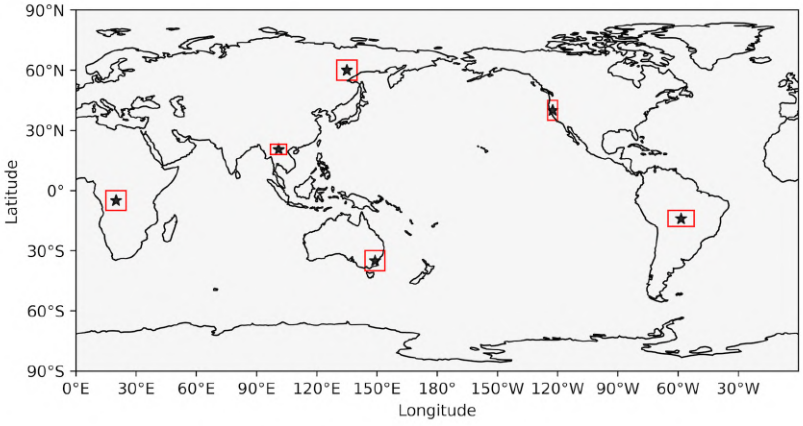

Figure 1. The wildfire regions we focused on are shown as red squares. The latitude and longitude of these six regions are defined in Table 1.

Table 1. The regions and periods of extreme global wildfires from 2018 to 2021.

Country / State	Longitude [°]	Latitude [°]	Month and Year
Amazon	52°W-65°W	10°S-18°S	Sep. 2020
Angola	15°E-25°E	0°S-10°S	Aug. 2020
Australia	144°E-154°E	30°S-40°S	Dec. 2019 - Jan. 2020
California	120°W-125°W	35°N-45°N	August 2018
			Jul. 2021
			Aug. 2020 - Sep. 2020
Southeast Asia	97°E-105°E	18°N-23°N	Mar. 2020 - Apr. 2020
Siberia	130°E-140°E	55°N-65°N	Aug. 2020
			Jul. 2021

https://doi.org/10.5194/egusphere-2022-21
Preprint. Discussion started: 28 March 2022

2.2 Copernicus global land service: CGLS-LC100

The Copernicus Global Land Service (CGLS) delivers an annual dynamic global Land Cover product with 100 m spatial resolution (CGLS-LC100) (Buchhorn et al., 2020). There are 23 classifications aligned with the Food and Agriculture Organization of the United Nations's Land Cover Classification System. In this study, we use the CGLS-LC100 data of 2019 with overall mapping accuracy of 80.3%, to investigate the vegetation type of each wildfire site.

2.3 Japan Meteorological Agency / Global objective analysis data

The Japan Meteorological Agency (JMA) is a Japanese agency that collects and reports weather, aviation, and oceanographic data and provides them to the public. The global analysis (GANAL) data provided by JMA includes the meteorological variables such as temperature, humidity, and wind speed for the different barometric pressures obtained by assimilating numerical predicted and observed values. In this study, we use the 1-degree mesh GANAL data of relative humidity during the fire period of each wildfire site. It was confirmed that the fire smoke is generally distributed several kilometers from the ground by some LIDAR observations (Val Martin et al., 2010; Paugam et al., 2016; Yao et al., 2018). We used the average relative humidity in the lower atmosphere from the ground surface to about 1 km altitude (925 hPa).

3 Results

3.1 Time-series analysis of aerosol optical properties

First, we calculated the monthly variation of AOT (500 nm), AE (380-500 nm), and SSA (380 nm) retrieved by GCOM-C SGLI products, using the mean pixel values for the six wildfire regions given in Table 1. As shown in Fig. 2, the period of high AOT almost coincided with the timing of wildfire events. This AOT variation suggests that the significant increase in aerosols due to wildfire lasts approximately three months in any region. Note that the AOT values for Siberia during winter (from December to April) were not plotted to avoid the contamination due to the high reflectance of the ice/snow cover (e.g., Wei et al., 2018). A large AE was observed during extensive AOT periods, such as California in August 2020 and July 2021 and Siberia in July 2021. This suggests that the aerosol particles emitted from biomass burning are smaller than those in the no-fire periods in these areas. In addition, there seem to be negative correlations between AOT and SSA everywhere except for Siberia in July 2021. This behavior of SSA during wildfires indicates that increased biomass burning aerosols may enhance the light absorption effect of aerosols, which is consistent with the previous studies (Liu et al., 2015; Cheng et al., 2016). This might be because biomass burning is one of the largest sources of black carbon emissions into the atmosphere. To estimate the impact of these biomass burning aerosols on radiative forcing and global warming, it is necessary to calculate the total outgoing shortwave flux changes over the fire and non-fire periods, discussed in Section 3.5.

https://doi.org/10.5194/egusphere-2022-21
Preprint. Discussion started: 28 March 2022

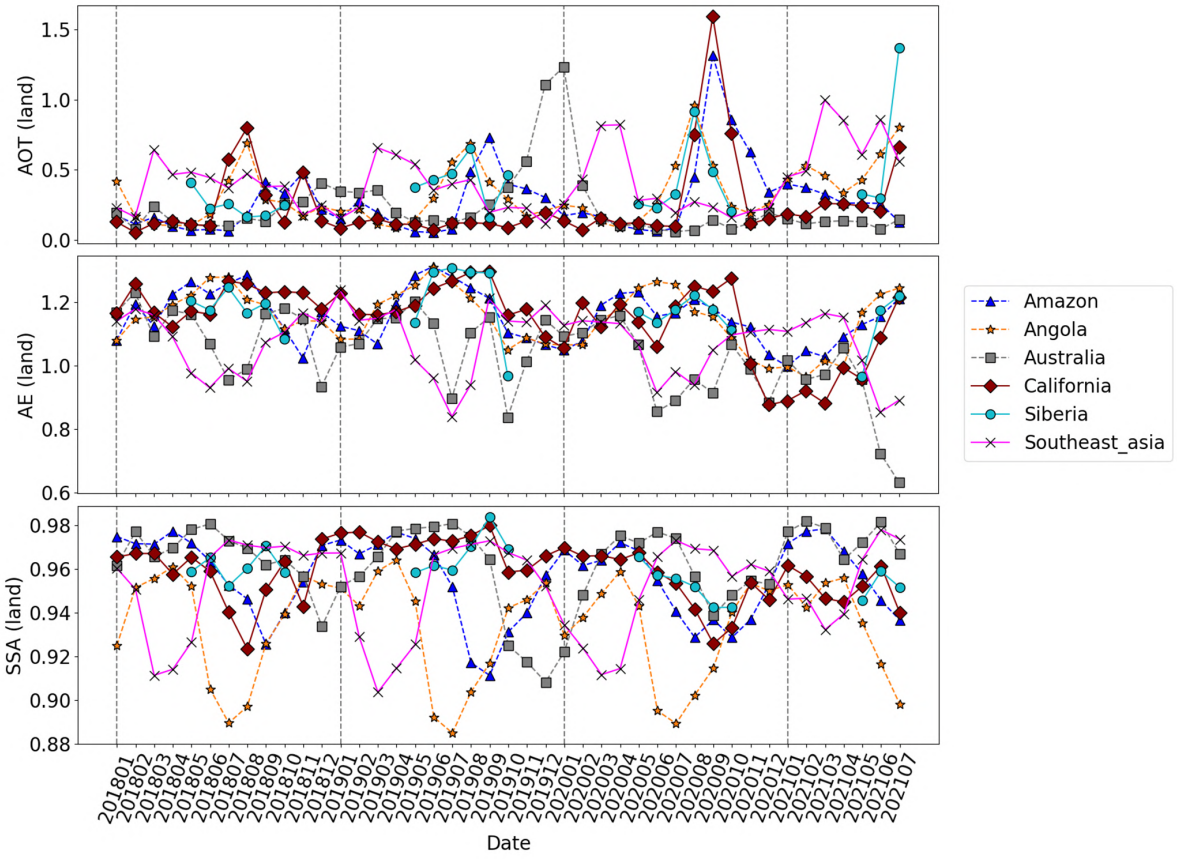

Figure 2. The monthly averaged variation of aerosol optical properties from 2018 to 2021 per the GCOM-C SGLI aerosol product. The wildfire regions are specified in Fig. 1 and Table 1. The top, middle, and bottom panels are AOT over land (500 nm), AE over land (380-500 nm), and SSA over land (380 nm), respectively. The different-colored plots represent different regions as noted in the legend. The data for the northern and southern hemispheres are plotted as solid and dashed lines, respectively.

3.2 Comparison of single scattering albedo and Ångström exponent

Next, we focused on SSA and AE relations during a wildfire to understand the similarities and differences in aerosol properties for each fire event. Fig. 3 shows the relation between monthly averaged SSA and AE during the high-severity fire periods. We used only high AOT pixels (AOT $\geq$ 1.0) to extract the pure components of the fire smokes. The spatially averaged plots for each event indicate that there seems to be a weak positive correlation between SSA and AE among the global wildfire events. In other words, a large SSA is observed where the size of biomass burning aerosol is small (i.e., large AE). One reason for this trend might be Mie theory scattering, in which the SSA becomes larger as the smaller size parameter for the constant complex refractive index ($\lesssim 0.1$) becomes smaller (Mie, 1908; Moosmuller and Sorensen, 2018). The chamber study and aircraft measurements study also show that the SSA decreases as the dust aerosol size fraction increases due to the absorbing

https://doi.org/10.5194/egusphere-2022-21
Preprint. Discussion started: 28 March 2022

effect of the larger particles (Di Biagio et al., 2019; Ryder et al., 2013). However, this relationship is valid over a relatively large particle size range from the transition regime to the geometric regime (a few size parameters). Since the biomass burning aerosols also contain smaller particles, the positive correlation between SSA and AE in Fig. 3 might originate for another reason or by coincidence (actually the relatively high p-value of 0.10 was obtained). When we locally focused on the aerosol properties in each region (small dots in Fig. 3), the correlations seemed to be negative. As shown in Table 2, the slopes obtained by fitting the values of all pixels in each observed region individually with simple linear functions are negative in all regions, whereas the slopes are positive when fitting all the averages of each event. The reason for this modest negative correlation for the events might be explained by hygroscopic growth. According to air sampling measurements (Titos et al., 2014), aerosol particles can take up water and become larger (i.e., smaller AE). Hence, the ratio of scattering cross section to extinction cross section becomes larger (i.e., larger SSA). Also, Spearman's rank correlation coefficients (CC_{sp}) in arid areas and seasons such as Australia and California fire events are much weaker ($|CC_{\mathrm{sp}}| < 0.2$) than that in the Amazon, Angola, Siberia, and Southeast Asia.

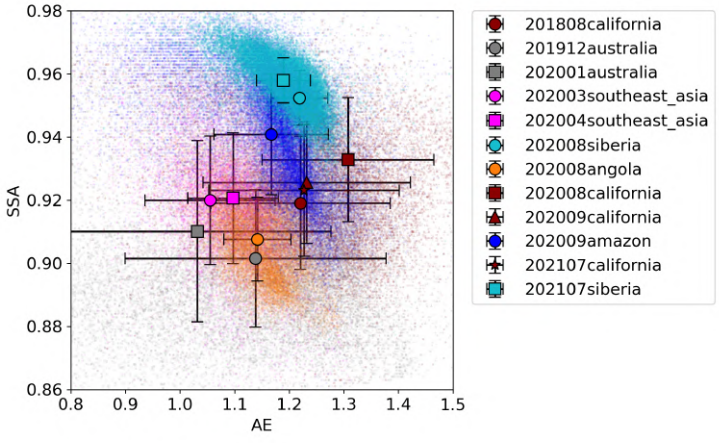

Figure 3. Monthly averaged SSA (380 nm) and AE (380-500 nm) relation for extreme global wildfires. Only high AOT (≥ 1.0) pixels are used. The large filled plots represent the spatial averages and standard deviations for the regions defined in Table 1. All pixel data in each region are also plotted as small dots with a corresponding color labeled in the legend.

3.3 Relative humidity and vegetation type

To investigate the origins of the difference in SSA and AE distributions in different regions more precisely, we analyzed the relative humidity in each region using GANAL data provided by JMA. The left panel of Fig. 4 shows that the relationship between AE and relative humidity, showing a negative correlation (CC_{sp} is -0.65 and the p-value is 0.02). This means that larger particles are observed in regions with higher relative humidity, suggesting that the aerosols from biomass burning take up water and increase in size. According to Kasten (1969) and Hänel (1976), the dependence of particle size on relative humidity

https://doi.org/10.5194/egusphere-2022-21
Preprint. Discussion started: 28 March 2022

Table 2. The linear fitting results with the AE and SSA data for each wildfire event.

Country / State	Slope a	Intercept b	CC_{sp}	p-value
All regions	0.097 ± 0.061	0.813 ± 0.071	0.50	0.10
Amazon	-0.090 ± 0.001	1.046 ± 0.001	-0.56	< 0.05
Angola	-0.105 ± 0.001	1.027 ± 0.002	-0.43	< 0.05
Australia	-0.009 ± 0.001	0.916 ± 0.001	-0.003	0.60
California	-0.028 ± 0.001	0.959 ± 0.001	-0.19	< 0.05
Siberia	-0.099 ± 0.001	1.074 ± 0.001	-0.67	< 0.05
Southeast Asia	-0.074 ± 0.002	0.999 ± 0.002	-0.30	< 0.05

The slopes and intercepts were obtained by fitting the data for each wildfire event (SSA and AE) with a linear function, $SSA = aAE + b$. The Spearman's rank correlation coefficients CC_{sp} and p-value were also calculated. The averaged SSA and AE values of whole events are described in the All regions row.

can be approximately described by the **empirical formula**:

$$r \simeq r_0(1-f)^{-\epsilon}, \tag{1}$$

where r is the particle radius at relative humidity f, r_0 is the particle radius of dry matter, and ϵ is the constant depending on the composition of the aerosols. In this case, we assumed three types of aerosols (urban aerosols, sea-spray aerosols, and Sahara desert dust) and calculated the size ratio variation using the ϵ values obtained by measuring the physical properties of aerosol particles (Hänel, 1972). The particle size gradually increases up to relative humidity of $f \simeq 80\%$, and rapidly grows up above that as shown in Fig 5. The satellite-based result in Fig. 4 shows a modest trend of particle growth up to the relative humidity of $f \simeq 80\%$, supporting this empirical formula.

The SSA and relative humidity relation is more complicated, as shown in the right panel of Fig. 4. It seems that there was no correlation (in fact, the obtained correlation coefficient was $CC_{\mathrm{sp}} = 0.22$ and the p-value was 0.48). Based on a field study (Titos et al., 2014) and Mie theory, however, SSA is expected to increase as the relative humidity increases due to hygroscopic growth, which decreases the imaginary part of the refractive index because the absorption of water particles is weak at visible wavelengths. To reveal why no clear correlation was found between SSA and relative humidity, we investigated the vegetation type at the origins of the aerosols. The difference in composition of aerosols can also significantly affect aerosol properties. The percentages of land cover types at the hotspots that could be source vegetation of aerosol emissions are shown in Fig 6, using the CGLS land cover data and GCOM-C SGLI hotspots detection data. Based on this result, we classified the fire events into two groups by their most dominant vegetation types: needle-leaf forests in California and Siberia and broadleaf forests in the Amazon, Angola, Australia, and Southeast Asia. Along with this grouping, the linear fitting with the relation between SSA and relative humidity for each group independently shows a significant increase in the correlation coefficient to $CC_{\mathrm{sp}} = 0.94$ (needle-leaf forest) and $CC_{\mathrm{sp}} = 0.83$ (broadleaf forest), respectively. Furthermore, the obtained p-values were less than 0.05 for both needle-leaf and broadleaf forests. Therefore, we found a positive correlation between SSA and relative humidity,

https://doi.org/10.5194/egusphere-2022-21
Preprint. Discussion started: 28 March 2022

considering the vegetation difference. For both vegetation groups, this trend of increase in SSA might have originated in the hygroscopic growth as mentioned above.

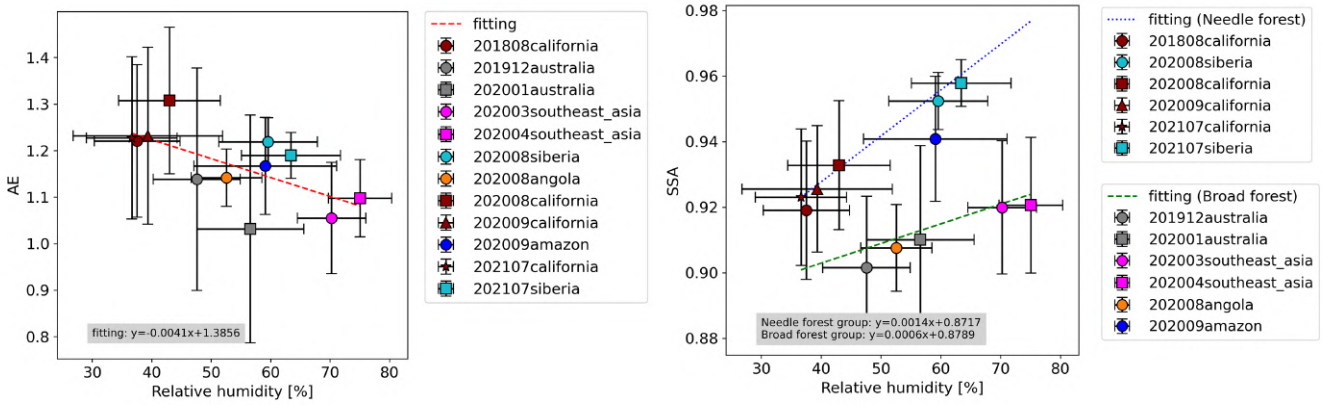

Figure 4. Monthly averaged AE vs. relative humidity (left panel) and SSA vs. relative humidity (right panel). The used pixels are extracted from high AOT ($\geq$ 1.0) regions.

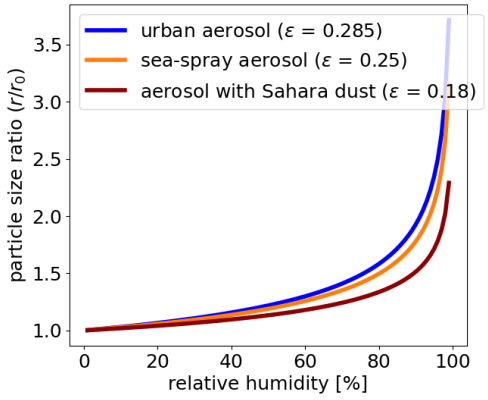

Figure 5. The particle size ratio vs. relative humidity for three types of aerosols: urban aerosol, sea-spray aerosol, and maritime aerosol containing Saharan dust.

3.4 Aging effect of the aerosols

165 The previous sections suggested that the optical properties of aerosols in wildfires depend mainly on the local relative humidity and vegetation type. In this section, we investigate the temporal variation of particle size to find the cause of the negative

https://doi.org/10.5194/egusphere-2022-21
Preprint. Discussion started: 28 March 2022

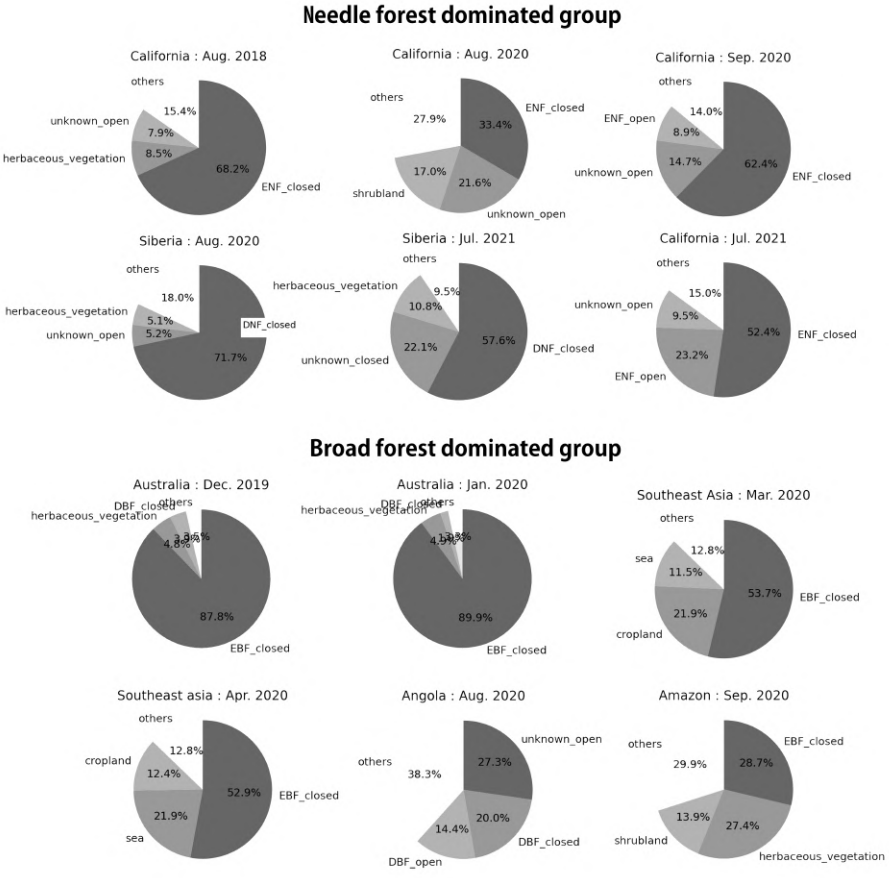

Figure 6. Land use and land cover types at the hotspots for each event using the satellite-based product (CGLS-LC100).

correlations shown for each fire event in Fig. 3. We show the GCOM-C SGLI satellite images (true color RGB and AOT (500 nm) images) in the left two panels of Fig. 7, at the events of Australia, Southeast Asia, Siberia, the Amazon and California on the dates when the fire smoke flow is easily visible. The fire event in Angola was not analyzed because it was challenging to identify the plume flow (the fire smoke is widely spread out). The several $1^\circ \times 1^\circ$ rectangles shown in the AOT images of Fig. 7 are defined with the smoke flow for each image, starting from the hotspots. The hotspots' locations are determined using the GCOM-C SGLI's wildfire product as described in Section 2, and if no hotspots were detected, the starting position was determined by visually examining the RGB image. The AE and SSA averages within each rectangle are plotted against the distance from the center coordinate of the first rectangle in the three right panels of Fig. 7. Because the distance from the hotspots is roughly proportional to the time elapsed since the smoke was generated, we can discuss the temporal changes in the properties of smoke particles in this analysis. The results show that the smoke particle size increases (i.e., AE decrease) with time in almost all locations, which indicates that the process of hygroscopic growth was observed. However, the characteristics of California are partially different from other regions, as the particle size decreases beyond $\sim 4^\circ$ rom the hotspot area. Since the

https://doi.org/10.5194/egusphere-2022-21
Preprint. Discussion started: 28 March 2022

humidity in California was extremely low compared to other regions during the fire period, it was assumed that the hygroscopic growth stopped at a certain size. Then, a simple trend toward smaller particles to be blown farther away was observed. At the California fire on 23 July 2021, the AE in the region close to the hotspots was more than 1.3, indicating that the particle size was smaller than the others. The reason for this might be its low relative humidity or the low initial concentrations of aerosols and low coagulation rates just after emission due to predominantly flaming combustion of crown fuels (Nikonovas et al., 2015).

From the above, the aerosols especially in highly humid areas easily grow in size by water uptake. Large aerosol particles containing much water generally have high SSA because the absorption in the visible spectrum of water particles is weak (Titos et al., 2014). Moreover, the trend to move from the lower right to the upper left over time, as seen in the rightmost panel of Fig. 7, explains the negative correlation between SSA and AE obtained for each fire event in Fig. 3. It is suggested that local differences in the characteristics of aerosols generated by wildfires depend highly on the relative humidity in each region and reflect time-series changes in particle size.

3.5 Estimation of radiative forcing

It has been reported that the black carbon aerosols emitted from wildfire might amplify the heating effect, especially in a snow-covered area such as the Arctic zone, due to the enhancing absorption of sunlight, which promotes melting and causes positive climate warming feedback (Li et al., 2016; Kostrykin et al., 2021). On the other hand, in other regions, ground-based and satellite-based studies have reported that the net radiative forcing of the biomass burning aerosols could be negative, considering the direct effects of aerosols (Pani et al., 2016; Zhuravleva et al., 2017; Chang et al., 2021). The differences in aerosol optical properties of the wildfires described in Section 3 could substantially affect radiative forcing. Therefore, we estimated the radiative forcing for extreme fire events. Although the effects of aerosols on radiative forcing are categorized as direct and indirect, we focused on the direct effect of aerosols to investigate the impact of the short-lived climate forcer in this study. To estimate the direct effects of aerosols that influence the radiative forcing on a relatively short time scale, we focus on pixels for only clear skies and compare the shortwave radiation within the fire and base (non-fire) periods. However, when extracting clear-sky pixels, pixels containing heavy aerosols are often misclassified as clouds even if it is clear (e.g., Brennan et al., 2005; Sun et al., 2011). To avoid the misclassification between aerosols and clouds, we applied a deep neural network method to detect the clear-sky pixels using the LTOA product (Nakajima et al., 2019; Tanada, 2021). It should be noted that this simple method to compare the shortwave radiation during the fire and base periods at the clear-sky pixels includes the effects of the land surface albedo changes arising from vegetation burning in addition to the aerosol direct effects. This problem is discussed later.

First, we calculated the TOA radiance spectra from 380 nm to 2.21 μm, which were obtained from SGLI's 13 wavelength channels (380 nm, 412 nm, 443 nm, 490 nm, 530 nm, 565 nm, 673.5 nm, 763 nm, 868.5 nm, 1.05 μm, 1.38 μm, 1.63 μm, and 2.21 μm), for the fire and base periods in California as shown in Fig. 8. Since the original reflectance is quite different between land and ocean, the spectra were calculated separately over land and ocean. Three images over each land (top) and ocean (bottom) show the 10-day averaged spectra in time series (from left to right), where the center image shows the spectrum when the most large-scale smoke was detected during the fire period. We defined the fire period from August 2020 to October 2020

https://doi.org/10.5194/egusphere-2022-21
Preprint. Discussion started: 28 March 2022

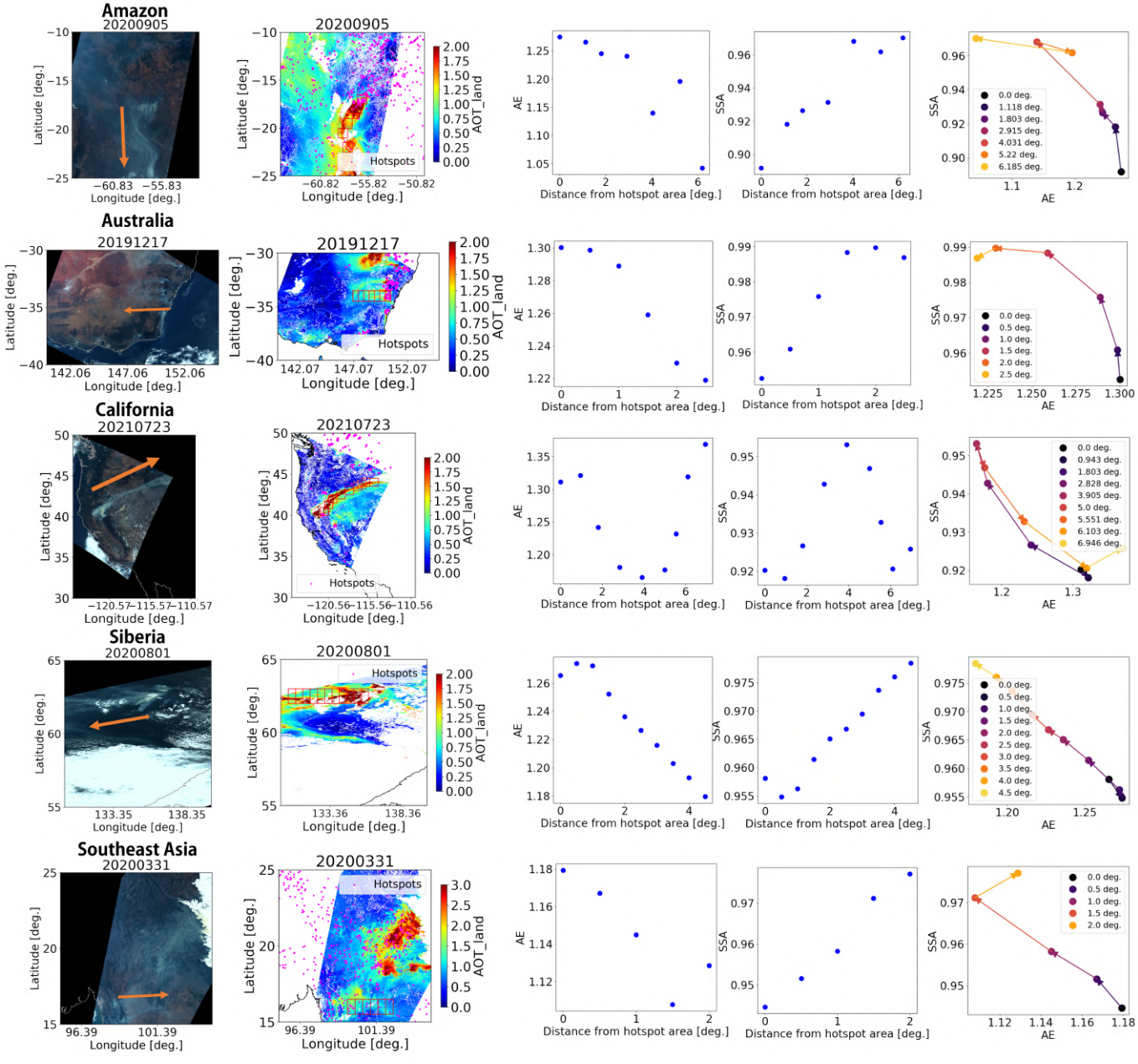

Figure 7. True color RGB and AOT (500 nm) images are displayed in the left two panels. The smoke spread directions are represented by orange arrows in the RGB images. The filled magenta circles in the AOT images represent the hotspots detected for the past three days by GCOM-C SGLI's wildfire product using thermal infrared sensors. The right three panels show AE (380-500 nm) vs. distance from hotspot area, SSA vs. distance from hotspot area, and the relation between SSA and AE with time variation, respectively. The AE and SSA extraction regions are the open red squares in the AOT images.

https://doi.org/10.5194/egusphere-2022-21
Preprint. Discussion started: 28 March 2022

and the base period from August 2019 to October 2019 (with almost no fires), exactly one year before the fire period. Over the ocean, we found a significant difference in the shortwave radiance, as shown in the center bottom image in Fig. 8. On the other hand, the spectral difference is much smaller for the burning aerosols over the land. Next, we calculated the time series of the difference between the fire and base periods' shortwave radiation calculated by integrating the linearly complemented radiance spectrum from 380 nm to 2.21 μm for wavelength and solid angle as:

$$RF_{\mathrm{SW}} = \pi \left[\int L_{\mathrm{TOA}}^{\mathrm{base}}(\lambda) d\lambda - \int L_{\mathrm{TOA}}^{\mathrm{fire}}(\lambda) d\lambda \right], \tag{2}$$

where RF_{SW} is the net incoming shortwave radiation at TOA during the fire period (i.e., radiative forcing), $L_{\mathrm{TOA}}^{\mathrm{base}}(\lambda)$ and $L_{\mathrm{TOA}}^{\mathrm{fire}}(\lambda)$ are the observed radiance at the top of the atmosphere during the base and fire periods, respectively. As shown in Fig. 9, the shortwave radiation is not strongly dependent on the satellite viewing angle over both land and ocean. Thereby, when integrating with respect to solid angle, we assumed that the ground surface was a Lambert surface (Gristey et al., 2021). To account for the difference in solar zenith angle, the radiation observed during the base period was corrected using the averaged solar zenith angle during the fire period. Although it is not as accurate as integrating the actual continuous spectrum compared with linearly complementing each SGLI's channel, we chose this simple way to grasp the general trend of the spectrum changes between fire and base periods. As expected from Fig. 8, the radiative forcing over the ocean is significantly negative (~ 100 Wm^{-2}: cooling effect) when the fire is most intense (around 15 September), as shown in Fig. 10. This might be because the ocean originally has lower reflectance in a broad spectrum than land, so the difference is more pronounced when the fire smoke covers the ocean. Table 3 shows the estimated radiative forcing for the Amazon, Angola, Siberia, Australia, and Southeast Asia using the same method as for the California fire. The fire and base periods were determined with the time variability of the AOT in Fig. 2, and we chose the same month in a different year (except for Angola and Southeast Asia because the fires occurred in the same season every year from 2018 to 2021 in these areas) As a result, the radiative forcing is a negative constant ~ -10 Wm^{-2} over land for every region. This suggests that the immediate impact on the radiative forcing is weak for the burning aerosols over land. Considering the land surface reflectance and NDVI (Normalized Difference Vegetation Index) in regions averaged over the base period as shown in Table 4, there was no apparent difference in radiative forcing due to the difference in the land surface albedo. The smoke spread over the ocean from the fires, resulting in large negative radiative forcing estimated at -76.6, -96.7 Wm^{-2} for the fires in California and Australia, respectively. Because the incident solar radiation was not equal with the different solar zenith angles during each fire, we normalized RF_{SW} with a solar zenith angle of 60° for all events, and the results are shown in parentheses in the RF_{SW} columns of Table 3. Considering the difference in the optical properties obtained in Fig. 3, the fire smoke in Siberia is thought to have a larger SSA than other regions, i.e., more sunlight is reflected to space, suggesting a smaller **net** incoming radiation. However, we found no significant difference among the six regions regarding the net incoming radiation over the land. In addition, as can be seen from the discrete values for land and oceans, the primary contributor to the difference in radiative forcing would be the difference in the reflectances of the surface under the fire aerosols. As previously mentioned, RF_{SW} over land includes not only the direct aerosol effect but also the effect of the albedo changes of the land surface caused by fire. Therefore, we estimated the radiative forcing arising from the land surface albedo change separately, as shown in the rightmost column of Table 3 (RF_{SW} - albedo change). The

https://doi.org/10.5194/egusphere-2022-21
Preprint. Discussion started: 28 March 2022

RF_{SW} for the albedo changes was calculated in the same way using Eq. 2 for pixels where NDVI decreased by more than 3 σ from the mean and where AOT (500 nm) was less than 0.1, which is considered to be less affected by smoke Note that RF_{SW} - albedo change is normalized by the used pixel area ratio to compare with total radiative forcing over land (RF_{SW} - land). Vegetation burning, which decreases surface reflectance, contributed to the positive but faint radiative forcing. In any case, the direct effects of aerosols on short time scales contribute to negative radiative forcing over both land and ocean in localized areas around the wildfires.

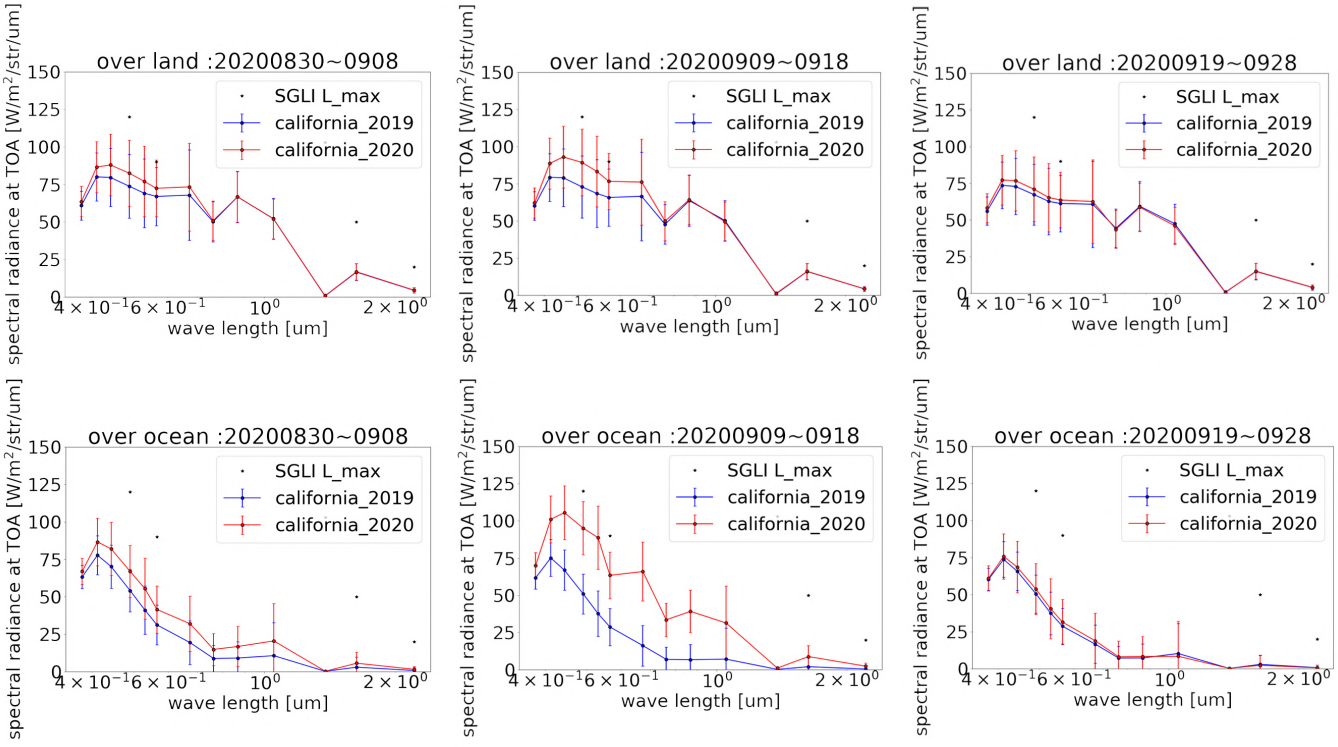

Figure 8. The TOA radiance spectra in California over land (upper panel) and ocean (lower panel) in time series (from left to right). Each radiance is calculated by averaging the pixel values in the region of interest, as given in Table 1. The error bars represent the standard deviation of the pixels in the region. The red and blue plots represent the spectra during the fire periods from August 2020 to September 2020 and base periods from August 2019 to September 2019, respectively. The black stars represent the maximum observable radiance for each channel of GCOM-C SGLI.

4 Discussion & Conclusion

In this paper, we systematically investigate the optical properties of aerosols generated by the large wildfires from 2018 to 2021 using GCOM-C satellite data. We found that the aerosol optical properties are different for each fire event, reflecting the local

https://doi.org/10.5194/egusphere-2022-21
Preprint. Discussion started: 28 March 2022

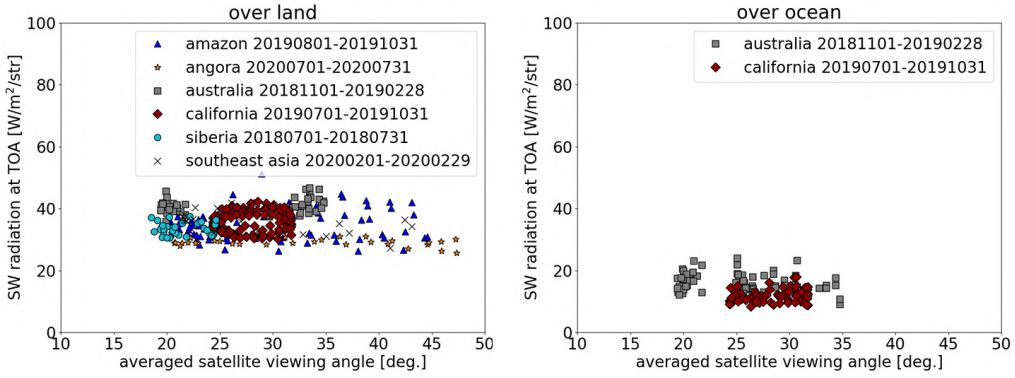

Figure 9. The relationship between the daily spatial averaged shortwave radiation and daily spatial averaged satellite viewing angle for six regions during no-fire periods, including base periods. Only clear-sky pixels over land (left panel) and ocean (right panel) were used to calculate the shortwave radiation.

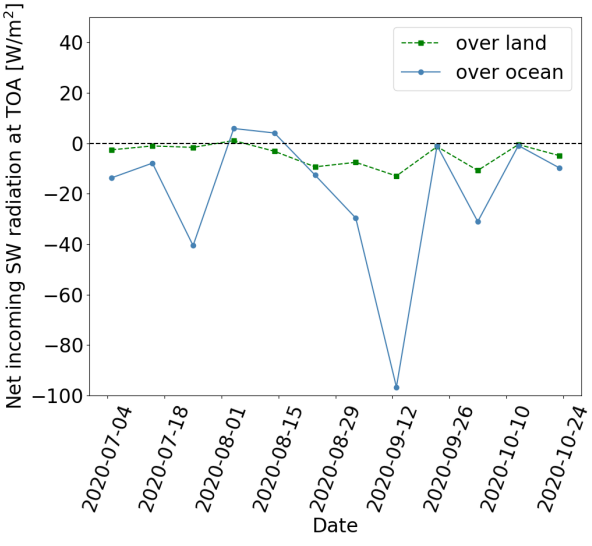

Figure 10. The time series of 10-day-averaged net incoming radiation for the California fire was calculated by subtracting the shortwave radiation during the base period from that during the fire period described by Eq. 2.

https://doi.org/10.5194/egusphere-2022-21
Preprint. Discussion started: 28 March 2022

Table 3. The net incoming radiation during the most intense fire periods for the world's six fire events.

Country / State	Base period	Fire period	RF_{SW} - land [$\mathrm{Wm^{-2}}$]	RF_{SW} - ocean [$\mathrm{Wm^{-2}}$]	RF_{SW} - albedo change [$\mathrm{Wm^{-2}}$]
Amazon	10-19 Sep. 2019	10-19 Sep. 2020	-12.9 (-7.6)	-	0.04 (0.02)
Angola	11-20 Sep. 2020	11-20 Aug. 2020	-21.1 (-12.3)	-	0.01 (0.01)
Australia	31 Dec. 2018 - 9 Jan. 2019	31 Dec. 2019 - 9 Jan. 2020	-10.9 (-6.3)	-76.6 (-44.1)	0.04 (0.02)
California	9-18 Sep. 2019	9-18 Sep. 2020	-13.0 (-8.0)	-96.7 (-59.6)	0.02 (0.01)
Siberia	11-20 July 2018	11-20 July 2021	-7.4 (-5.1)	-	0.10 (0.07)
Southeast Asia	11-20 Feb. 2020	11-20 March 2020	-1.5 (-0.9)	-	0.05 (0.03)

Net incoming radiation (RF_{SW} -land and -ocean) was calculated by subtracting the shortwave radiation of the fire period from the base (non-fire) period. RF_{SW} -albedo change is the contribution of the land surface albedo changes due to the fire to the net radiative forcing. The values inside the parentheses in the column of RF_{SW} are the normalized radiation for a solar zenith angle of 60°.

Table 4. The land surface reflectance during the base period.

Country / State	Surface reflectance at 673 nm	Surface reflectance at 1.05 μm	NDVI
Amazon	0.09	0.31	0.55
Angola	0.06	0.27	0.64
Australia	0.16	0.34	0.36
California	0.15	0.29	0.32
Siberia	0.04	0.27	0.74
Southeast Asia	0.05	0.21	0.62

Atmospherically corrected land surface reflectances at 673 nm and at 1.05 μm were averaged over the base period, calculated using GCOM-C SGLI's surface reflectance product. NDVI is calculated by $(R_{\mathrm{NIR}} - R_{\mathrm{red}})$ / $(R_{\mathrm{NIR}} + R_{\mathrm{red}})$, where R_{NIR} is surface reflectance at 1.05 μm, and R_{red} is surface reflectance at 673 nm.

climate and the original vegetation types. The highest AE (380-500 nm) was ~ 1.3 observed in California in August 2020, whereas the lowest values of AE (380-500 nm) ~ 1.0 were observed in Australia in January 2020 and Southeast Asia in March 2020. Thus, the particle size of the fire aerosols in California was smaller than at other sites. The highest observed SSA (380 nm) was ~ 0.96 in Siberia in July 2021, which is almost consistent with the ground-based analysis of the boreal forest fire (Eck et al. (2009): ~ 0.96 at 440 nm). This high SSA value implies a low black carbon fraction (i.e., a small imaginary part of the refractive index). In comparison, the lowest observed SSA (380 nm) is ~ 0.90 in Australia in December 2019, suggesting that the smoke contained more black carbon than the Siberia fire.

The global wildfires' overall SSA and AE mapping revealed that each fire event had a regional characteristic. In addition, the aerosol characteristic of each fire event depended on the relative humidity and the vegetation type in each region. The negative correlation between SSA and AE for some regions can be explained by hygroscopic growth. These results suggest that it is necessary to consider the regional optical characteristics and aging effect of biomass burning aerosols in addition to the basic

https://doi.org/10.5194/egusphere-2022-21
Preprint. Discussion started: 28 March 2022

parameters such as frequency of fires and amount of the aerosols in models when predicting and estimating the impact of wildfires on the climate and meteorology.

In Section 3.5, we estimated the instantaneous radiative forcing on short time scales for each fire. The obtained values are negative for all regions: from -21.1 to -1.5 W m^{-2} over land and -96.7 to -76.6 W m^{-2} over the ocean. According to the GFED4 analysis, the global average fire emissions were estimated to be 2.2 Pg C yr^{-1} from 1997 to 2016 (van der Werf et al., 2017). After subtracting the effect of CO_2 absorption by vegetation regrowth, the net greenhouse gas emission is 0.6 Pg C yr^{-1}, which is equivalent to about 6 % of the global fossil-fuel CO_2 emissions in 2014 (Boden et al., 2017). The model analysis (Ward et al., 2012), using the modified form of the Community Land Model (CLM) (2010kloster et al., 2010; Kloster et al., 2012), suggests that the annual global radiative forcing of CO_2 originated in wildfires is 0.83 Wm^{-2}, 0.62 Wm^{-2}, and 0.75 Wm^{-2} in 1850, 2000, and 2100, respectively. Compared to the global effect of CO_2 on radiative forcing, the direct effect of aerosols calculated in this study is local and instantaneous. However, it is large for negative forcing, particularly over the ocean. As we have seen, the aerosol optical properties and the effect on radiative forcing differ for each fire event. Especially when the area is near the ocean, the fire plume flows over the ocean, and its contribution to radiative forcing is seven to nine times that on the land, where we focused on in this study. Unlike the CO_2, which can remain in the atmosphere for centuries, short-lived climate forcers such as black carbon and organic carbon have a short life span and do not spread globally. Although the maximum transport distance of aerosols was several thousand kilometers in the case of the wildfires in California and Australia analyzed in this study, it was from several hundred to a thousand kilometer in most cases. Therefore, it is important to estimate the influence of biomass burning aerosols on the climate regionally. As reported by recent studies (Marle et al., 2017; Hoesly et al., 2018), the regional approach reveals that the amount of emission and the historical trend are different for each of the over 10 regions they divided the world into.

This study estimated the regional and instantaneous impacts on the radiative forcing at TOA during a fire by aerosol direct effect and surface albedo change. However, we also needed to consider the aerosol indirect effect on cloud formations over a longer time. Besides, regarding the effect of land surface albedo changes, the radiative forcing is positive for a few months after burning. After that, it becomes slightly negative for a few decades as the secondary vegetation with higher reflectance replaces the previous one, according to the global model simulation (Ward et al., 2012). The GCOM-C will continue to observe global climate changes for the long term. Thus, when the GCOM-C data is adequately accumulated in the future, we will discuss not only the instantaneous contribution of fires, but also medium and long term influence on the Earth's environment.

Code and data availability. The data and data analysis methods are available upon request.

Author contributions. Methodology, K.T.; investigation, K.T.; writing, K.T.; review and editing, H.M., T.H., M.Y. All authors have read and agreed to the published version of the manuscript.

https://doi.org/10.5194/egusphere-2022-21
Preprint. Discussion started: 28 March 2022

Competing interests. The authors declare that they have no conflict of interest.

Acknowledgements. The authors gratefully acknowledge the members of JAXA Earth Observation Research Center.

https://doi.org/10.5194/egusphere-2022-21
Preprint. Discussion started: 28 March 2022

References

Wavelength dependence of the optical depth of biomass burning, urban, and desert dust aerosols, Journal of Geophysical Research: Atmospheres, 104, 31 333–31 349, https://doi.org/https://doi.org/10.1029/1999JD900923, 1999.

2010kloster, S., Mahowald, N. M., Randerson, J. T., Thornton, P. E., Hoffman, F. M., Levis, S., Lawrence, P. J., Feddema, J. J., Oleson, K. W., and Lawrence, D. M.: Fire dynamics during the 20th century simulated by the Community Land Model, Biogeosciences, 7, 1877–1902, https://doi.org/10.5194/bg-7-1877-2010, 2010.

Arora, V. K. and Melton, J. R.: Reduction in global area burned and wildfire emissions since 1930s enhances carbon uptake by land, Nature Communications, 9, 1326, https://doi.org/10.1038/s41467-018-03838-0, 2018.

Boden, T. A., Andres, R. J., and Marland, G.: Global, Regional, and National Fossil-Fuel CO2 Emissions (1751 - 2014) (V. 2017), https://doi.org/10.3334/CDIAC/00001_V2017, 2017.

Brennan, J. I., Kaufman, Y. J., Koren, I., and Li, R.-R.: Aerosol-cloud interaction-Misclassification of MODIS clouds in heavy aerosol, IEEE Transactions on Geoscience and Remote Sensing, 43, 911–, 2005.

Buchhorn, M., Smets, B., Bertels, L., Roo, B. D., Lesiv, M., Tsendbazar, N.-E., Herold, M., and Fritz, S.: Copernicus Global Land Service: Land Cover 100m: collection 3: epoch 2019: Globe, https://doi.org/10.5281/zenodo.3939050, 2020.

Chang, D. Y., Yoon, J., Lelieveld, J., Park, S. K., Yum, S. S., Kim, J., and Jeong, S.: Direct radiative forcing of biomass burning aerosols from the extensive Australian wildfires in 2019¥textendash2020, Environmental Research Letters, 16, 044 041, https://doi.org/10.1088/1748-9326/abecfe, 2021.

Cheng, Y., Engling, G., Moosmuller, H., Arnott, W. P., Chen, L.-W. A., Wold, C. E., Hao, W. M., and bin He, K.: Light absorption by biomass burning source emissions, Atmospheric Environment, 127, 347–354, https://doi.org/https://doi.org/10.1016/j.atmosenv.2015.12.045, 2016.

Council, N. R.: Air Quality Management in the United States, The National Academies Press, Washington, DC, https://doi.org/10.17226/10728, 2004.

Dennison, P. E., Brewer, S. C., Arnold, J. D., and Moritz, M. A.: Large wildfire trends in the western United States, 1984–2011, Geophysical Research Letters, 41, 2928–2933, https://doi.org/https://doi.org/10.1002/2014GL059576, 2014.

Di Biagio, C., Formenti, P., Balkanski, Y., Caponi, L., Cazaunau, M., Pangui, E., Journet, E., Nowak, S., Andreae, M. O., Kandler, K., Saeed, T., Piketh, S., Seibert, D., Williams, E., and Doussin, J.-F.: Complex refractive indices and single-scattering albedo of global dust aerosols in the shortwave spectrum and relationship to size and iron content, Atmospheric Chemistry and Physics, 19, 15 503–15 531, https://doi.org/10.5194/acp-19-15503-2019, 2019.

Eck, T. F., Holben, B. N., Reid, J. S., Sinyuk, A., Hyer, E. J., O'Neill, N. T., Shaw, G. E., Vande Castle, J. R., Chapin, F. S., Dubovik, O., Smirnov, A., Vermote, E., Schafer, J. S., Giles, D., Slutsker, I., Sorokine, M., and Newcomb, W. W.: Optical properties of boreal region biomass burning aerosols in central Alaska and seasonal variation of aerosol optical depth at an Arctic coastal site, Journal of Geophysical Research: Atmospheres, 114, https://doi.org/https://doi.org/10.1029/2008JD010870, 2009.

Gillett, N. P., Weaver, A. J., Zwiers, F. W., and Flannigan, M. D.: Detecting the effect of climate change on Canadian forest fires, Geophysical Research Letters, 31, https://doi.org/https://doi.org/10.1029/2004GL020876, 2004.

Gristey, J. J., Su, W., Loeb, N. G., Vonder Haar, T. H., Tornow, F., Schmidt, K. S., Hakuba, M. Z., Pilewskie, P., and Russell, J. E.: Shortwave Radiance to Irradiance Conversion for Earth Radiation Budget Satellite Observations: A Review, Remote Sensing, 13, https://doi.org/10.3390/rs13132640, 2021.

https://doi.org/10.5194/egusphere-2022-21
Preprint. Discussion started: 28 March 2022

Hoesly, R. M., Smith, S. J., Feng, L., Klimont, Z., Janssens-Maenhout, G., Pitkanen, T., Seibert, J. J., Vu, L., Andres, R. J., Bolt, R. M., Bond, T. C., Dawidowski, L., Kholod, N., Kurokawa, J.-I., Li, M., Liu, L., Lu, Z., Moura, M. C. P., O'Rourke, P. R., and Zhang, Q.: Historical (1750–2014) anthropogenic emissions of reactive gases and aerosols from the Community Emissions Data System (CEDS), Geoscientific Model Development, 11, 369–408, https://doi.org/10.5194/gmd-11-369-2018, 2018.

Hänel, G.: Computation of the extinction of visible radiation by atmospheric aerosol particles as a function of the relative humidity, based upon measured properties, Journal of Aerosol Science, 3, 377–386, https://doi.org/https://doi.org/10.1016/0021-8502(72)90092-4, 1972.

Hänel, G.: The Properties of Atmospheric Aerosol Particles as Functions of the Relative Humidity at Thermodynamic Equilibrium with the Surrounding Moist Air, vol. 19 of *Advances in Geophysics*, pp. 73–188, Elsevier, https://doi.org/https://doi.org/10.1016/S0065-2687(08)60142-9, 1976.

Kasten, F.: Visibility forecast in the phase of pre-condensation, Tellus, 21, 631–635, https://doi.org/10.3402/tellusa.v21i5.10112, 1969.

Kloster, S., Mahowald, N. M., Randerson, J. T., and Lawrence, P. J.: The impacts of climate, land use, and demography on fires during the 21st century simulated by CLM-CN, Biogeosciences, 9, 509–525, https://doi.org/10.5194/bg-9-509-2012, 2012.

Kostrykin, S., Revokatova, A., Chernenkov, A., Ginzburg, V., Polumieva, P., and Zelenova, M.: Black Carbon Emissions from the Siberian Fires 2019: Modelling of the Atmospheric Transport and Possible Impact on the Radiation Balance in the Arctic Region, Atmosphere, 12, https://doi.org/10.3390/atmos12070814, 2021.

Li, Y., Chen, J., Kang, S., Li, C., Qu, B., Tripathee, L., Yan, F., Zhang, Y., Guo, J., Gul, C., and Qin, X.: Impacts of black carbon and mineral dust on radiative forcing and glacier melting during summer in the Qilian Mountains, northeastern Tibetan Plateau, The Cryosphere Discussions, 2016, 1–14, https://doi.org/10.5194/tc-2016-32, 2016.

Liu, S., Aiken, A. C., Gorkowski, K., Dubey, M. K., Cappa, C. D., Williams, L. R., Herndon, S. C., Massoli, P., Fortner, E. C., Chhabra, P. S., Brooks, W. A., Onasch, T. B., Jayne, J. T., Worsnop, D. R., China, S., Sharma, N., Mazzoleni, C., Xu, L., Ng, N. L., Liu, D., Allan, J. D., Lee, J. D., Fleming, Z., Mohr, C., Zotter, P., Szidat, S., and Prevot, A. H.: Enhanced light absorption by mixed source black and brown carbon particles in UK winter, Nature Communications, 6, 8435, https://doi.org/10.1038/ncomms9435, 2015.

Marle, M. v., Kloster, S., Magi, B., Marlon, J., Daniau, A.-L., Field, R., Arneth, A., Forrest, M., Hantson, S., Kehrwald, N., Knorr, W., Lasslop, G., Li, F., Mangeon, S., Yue, C., Kaiser, J., and Werf, G.: Historic global biomass burning emissions based on merging satellite observations with proxies and fire models (1750–2015), Geoscientific Model Development Discussions, pp. 1–56, https://doi.org/10.5194/gmd-2017-32, 2017.

Mie, G.: Beiträge zur Optik trüber Medien, speziell kolloidaler Metallösungen, Annalen der Physik, 330, 377–445, https://doi.org/10.1002/andp.19083300302, 1908.

Moosmuller, H. and Sorensen, C.: Single Scattering Albedo of Homogeneous, Spherical Particles in the Transition Regime, Journal of Quantitative Spectroscopy and Radiative Transfer, 219, https://doi.org/10.1016/j.jqsrt.2018.08.015, 2018.

Murakami, H.: GCOM-C/SGLI Land Atmospheric Correction Algorithm, https://suzaku.eorc.jaxa.jp/GCOM_C/data/ATBD/ver2/V2ATBD_T1A_BRDF_Murakami.pdf, 2020.

Nakajima, T. Y., Ishida, H., Nagao, T. M., Hori, M., Letu, H., Higuchi, R., Tamaru, N., Imoto, N., and Yamazaki, A.: Theoretical basis of the algorithms and early phase results of the GCOM-C (Shikisai) SGLI cloud products, Progress in Earth and Planetary Science, 6, 52, https://doi.org/10.1186/s40645-019-0295-9, 2019.

Nikonovas, T., North, P. R. J., and Doerr, S. H.: Smoke aerosol properties and ageing effects for northern temperate and boreal regions derived from AERONET source and age attribution, Atmospheric Chemistry and Physics, 15, 7929–7943, https://doi.org/10.5194/acp-15-7929-2015, 2015.

https://doi.org/10.5194/egusphere-2022-21
Preprint. Discussion started: 28 March 2022

Pani, S. K., Wang, S.-H., Lin, N.-H., Lee, C.-T., Tsay, S.-C., Holben, B. N., Janjai, S., Hsiao, T.-C., Chuang, M.-T., and Chantara, S.: Radiative Effect of Springtime Biomass-Burning Aerosols over Northern Indochina during 7-SEAS/BASELInE 2013 Campaign, 16, 2802–2817, https://doi.org/10.4209/aaqr.2016.03.0130, 2016.

Paugam, R., Wooster, M., Freitas, S., and ValMartin, M.: A review of approaches to estimate wildfire plume injection height within large-scale atmospheric chemical transport models, Atmospheric Chemistry and Physics, 16, 907–925, https://doi.org/10.5194/acp-16-907-2016, 2016.

Reinhard, M., Rebetez, M., and Schlaepfer, R.: Recent climate change: Rethinking drought in the context of Forest Fire Research in Ticino, South of Switzerland, Theoretical and Applied Climatology, 82, 17–25, https://doi.org/10.1007/s00704-005-0123-6, 2005.

Ryder, C. L., Highwood, E. J., Rosenberg, P. D., Trembath, J., Brooke, J. K., Bart, M., Dean, A., Crosier, J., Dorsey, J., Brindley, H., Banks, J., Marsham, J. H., McQuaid, J. B., Sodemann, H., and Washington, R.: Optical properties of Saharan dust aerosol and contribution from the coarse mode as measured during the Fennec 2011 aircraft campaign, Atmospheric Chemistry and Physics, 13, 303–325, https://doi.org/10.5194/acp-13-303-2013, 2013.

Schuster, G. L., Dubovik, O., and Holben, B. N.: Angstrom exponent and bimodal aerosol size distributions, Journal of Geophysical Research: Atmospheres, 111, https://doi.org/https://doi.org/10.1029/2005JD006328, 2006.

Shi, S., Cheng, T., Gu, X., Guo, H., Wu, Y., and Wang, Y.: Biomass burning aerosol characteristics for different vegetation types in different aging periods, Environment International, 126, 504–511, https://doi.org/https://doi.org/10.1016/j.envint.2019.02.073, 2019.

Stocker, T., Qin, D., Plattner, G.-K., Alexander, L., Allen, S., Bindoff, N., BreÌon, F.-M., Church, J., Cubasch, U., Emori, S., Forster, P., Friedlingstein, P., Gillett, N., Gregory, J., Hartmann, D., Jansen, E., Kirtman, B., Knutti, R., KrishnaÂ Kumar, K., Lemke, P., Marotzke, J., Masson-Delmotte, V., Meehl, G., Mokhov, I., Piao, S., Ramaswamy, V., Randall, D., Rhein, M., Rojas, M., Sabine, C., Shindell, D., Talley, L., Vaughan, D., and Xie, S.-P.: Technical Summary, book section TS, Cambridge University Press, Cambridge, United Kingdom and New York, NY, USA, https://doi.org/10.1017/CBO9781107415324.005, 2013.

Sun, W., Videen, G., Kato, S., Lin, B., Lukashin, C., and Hu, Y.: A study of subvisual clouds and their radiation effect with a synergy of CERES, MODIS, CALIPSO, and AIRS data, Journal of Geophysical Research: Atmospheres, 116, https://doi.org/https://doi.org/10.1029/2011JD016422, 2011.

Takaku, J.: GCOM-C/SGLI geometric correction algorithm, https://suzaku.eorc.jaxa.jp/GCOM_C/data/ATBD/ver1/V1ATBD_G2ABC_geo_Takaku_20200908.pdf, 2020.

Tanada, K.: Algorithm Theoretical Basis Document of GCOM-C/SGLI Ver.3 Cloud Flag Product (CLFG), https://suzaku.eorc.jaxa.jp/GCOM_C/data/ATBD/ver3/V3ATBD_A1ABC_CLFG_tanada.pdf, 2021.

Titos, G., Jefferson, A., Sheridan, P. J., Andrews, E., Lyamani, H., Alados-Arboledas, L., and Ogren, J. A.: Aerosol light-scattering enhancement due to water uptake during the TCAP campaign, Atmospheric Chemistry and Physics, 14, 7031–7043, https://doi.org/10.5194/acp-14-7031-2014, 2014.

Val Martin, M., Logan, J. A., Kahn, R. A., Leung, F.-Y., Nelson, D. L., and Diner, D. J.: Smoke injection heights from fires in North America: analysis of 5 years of satellite observations, Atmospheric Chemistry and Physics, 10, 1491–1510, https://doi.org/10.5194/acp-10-1491-2010, 2010.

van der Werf, G. R., Randerson, J. T., Giglio, L., van Leeuwen, T. T., Chen, Y., Rogers, B. M., Mu, M., van Marle, M. J. E., Morton, D. C., Collatz, G. J., Yokelson, R. J., and Kasibhatla, P. S.: Global fire emissions estimates during 1997–2016, Earth System Science Data, 9, 697–720, https://doi.org/10.5194/essd-9-697-2017, 2017.

https://doi.org/10.5194/egusphere-2022-21
Preprint. Discussion started: 28 March 2022

Ward, D. S., Kloster, S., Mahowald, N. M., Rogers, B. M., Randerson, J. T., and Hess, P. G.: The changing radiative forcing of fires: global model estimates for past, present and future, Atmospheric Chemistry and Physics, 12, 10 857–10 886, https://doi.org/10.5194/acp-12-10857-2012, 2012.

Wei, J., Sun, L., Peng, Y., Wang, L., Zhang, Z., Bilal, M., and Ma, Y.: An Improved High-Spatial-Resolution Aerosol Retrieval Algorithm for MODIS Images Over Land, Journal of Geophysical Research: Atmospheres, 123, 12,291–12,307, https://doi.org/https://doi.org/10.1029/2017JD027795, 2018.

Yamamoto, G. and Tanaka, M.: Increase of Global Albedo Due to Air Pollution, Journal of the Atmospheric Sciences, 29, 1405–1412, https://doi.org/10.1175/1520-0469(1972)029, 1972.

Yao, J., Raffuse, S. M., Brauer, M., Williamson, G. J., Bowman, D. M., Johnston, F. H., and Henderson, S. B.: Predicting the minimum height of forest fire smoke within the atmosphere using machine learning and data from the CALIPSO satellite, Remote Sensing of Environment, 206, 98–106, https://doi.org/https://doi.org/10.1016/j.rse.2017.12.027, 2018.

Yoshida, M.: Algorithm Theoretical Basis Document of aerosol by non-polarization for GCOM-C/SGLI, https://suzaku.eorc.jaxa.jp/GCOM_C/data/ATBD/ver2/V2ATBD_A3AB_ARNP_Yoshida.pdf, 2020.

Zhuravleva, T. B., Kabanov, D. M., Nasrtdinov, I. M., Russkova, T. V., Sakerin, S. M., Smirnov, A., and Holben, B. N.: Radiative characteristics of aerosol during extreme fire event over Siberia in summer 2012, Atmospheric Measurement Techniques, 10, 179–198, https://doi.org/10.5194/amt-10-179-2017, 2017.

Ångström, A.: On the Atmospheric Transmission of Sun Radiation and on Dust in the Air, Geografiska Annaler, 11, 156–166, http://www.jstor.org/stable/519399, 1929.